PHYSICAL REVIEW A **98**, 062517 (2018)

Fourier-transform spectroscopy, direct potential fit, and electronic structure calculations on the entirely perturbed (4) $^1\Pi$ state of RbCs

I. Klincare, A. Kruzins, M. Tamanis, and R. Ferber[*]
Laser Center, Department of Physics, University of Latvia, 19 Rainis Boulevard, Riga 1586, Latvia

E. A. Pazyuk and A. V. Stolyarov[†]
Department of Chemistry, Lomonosov Moscow State University, Leninskiye Gory 1/3, Moscow 119991, Russia

(Received 1 October 2018; published 26 December 2018; corrected 10 August 2022)

We perform a high-resolution Fourier-transform spectroscopic study of the (4) $^1\Pi$ state of the RbCs molecule by applying two-step (4) $^1\Pi \leftarrow A\,^1\Sigma^+ \sim b\,^3\Pi \leftarrow X\,^1\Sigma^+$ optical excitation followed by observation of the (4) $^1\Pi \rightarrow X\,^1\Sigma^+$ laser-induced fluorescence (LIF) spectra. In many LIF progressions the collision-induced satellite rotational lines are observed, thus increasing the amount of term values and allowing us to estimate the Λ-doubling effect in the (4) $^1\Pi$ state. The direct potential fit (DPF) of experimental term values of 777 rovibronic levels of both ^{85}RbCs and ^{87}RbCs isotopologues is performed by means of the robust weighted nonlinear least-squares method. The DPF analysis based on the adiabatic approximation and analytical expanded Morse oscillator potential reveals numerous regular shifts in the measured level positions. The spectroscopic studies of the (4) $^1\Pi$ state are supported by the electronic structure calculations including the potential energy curves of the singlet- and triplet-state manifold and spin-allowed transition dipole moments. The subsequent estimates of radiative lifetimes and corresponding vibronic branching ratios elucidate a dominant contribution of the (4) $^1\Pi \rightarrow A \sim b$ channel into the total radiative decay of the (4) $^1\Pi$ state. The relative intensity distributions simulated for (4) $^1\Pi \rightarrow X\,^1\Sigma^+$ LIF progressions agree well with their observed counterparts even for the profoundly shifted levels of the entirely perturbed (4) $^1\Pi$ state. To get insight into the origin of the intramolecular perturbations, the relevant spin-orbit- and L-uncoupling electronic matrix elements are evaluated.

DOI: 10.1103/PhysRevA.98.062517

I. INTRODUCTION

The heteronuclear RbCs molecule has become the focus of spectroscopic studies due to the rapid development of producing ultracold polar alkali-metal diatomics (see [1–5] and references therein). An issue of particular experimental complexity is connected with the transfer of molecules from the weakly bound triplet $a(1)\,^3\Sigma^+$ level, in which the molecules are created from the colliding ultracold atoms at long-range internuclear distances, to their deeply bound vibronic level of the singlet $X\,^1\Sigma^+$ ground state. An alternative method was applied in Ref. [3], where RbCs molecules in the $v'' = 0$ level of the $X\,^1\Sigma^+$ state were formed via short-range photoassociation through the deeply bound mixed (2) $^3\Pi$ state. Since in both methods the transfer processes are realized via optical transitions, the information on energy and radiative properties of excited states of mixed singlet-triplet nature might broaden the possibilities of efficient optical paths. Though the quantum chemistry calculations of excited electronic states of RbCs were performed for a wide range of energies (see [6–9]), the existing experiment-based information on their potential energy curves (PECs) is still quite limited. As far as highly excited states approaching the asymptotic limit Rb($5s$) + Cs($5d$) or higher are concerned (see Fig. 1), one can mention the molecular constants and Rydberg-Klein-Rees (RKR) potentials for (4, 5) $^1\Pi$ and (7) $^1\Sigma^+$ states obtained from fragmentary data on term values in Ref. [10]. Applying high-resolution resonance-enhanced two-photon ionization spectroscopy to a molecular beam made it possible to study (4–6) $^1\Sigma^+$, (3) $^1\Pi$, and (4) $^3\Pi$ states, though including only the lowest rotational levels (see [11–14]). A detailed study of the (4) $^1\Sigma^+$ state that included modeling of prospective optical cycles for producing ground-state ultracold species was performed in Ref. [15]. In our recent work [16] we studied the (3) $^1\Pi$ state of RbCs converging to the Rb($5s$) + Cs($5d$) asymptotic limit of separated atoms at about 18 400 cm^{-1}, as well as the (5) $^1\Sigma^+$ state converging to the Rb($5s$) + Cs($7s$) at about 22 400 cm^{-1}.

The present paper addresses the next excited (4) $^1\Pi$ state of the RbCs molecule converging to the Rb($4d$) + Cs($6s$) asymptotic limit at about 23 200 cm^{-1}. From the point of view of testing the *ab initio* calculation approaches, it is of additional interest to have more experiment-based information on the electronic states, which are converging to asymptotic limits that include a d-shell alkali-metal atom. Indeed, though spin-orbit splitting for Rb($4\,^2D$) is small, it still plays a profound role due to a strong configuration interaction with lower states converging to the asymptote that includes the Rb($5p$) limit. The only currently existing data on the (4) $^1\Pi$ state can be found in Ref. [10], where 38 experimental term values were obtained from high-resolution Fourier-transform (FT) spectra of laser-induced fluorescence (LIF) excited by

---

[*] ferber@latnet.lv
[†] avstol@phys.chem.msu.ru

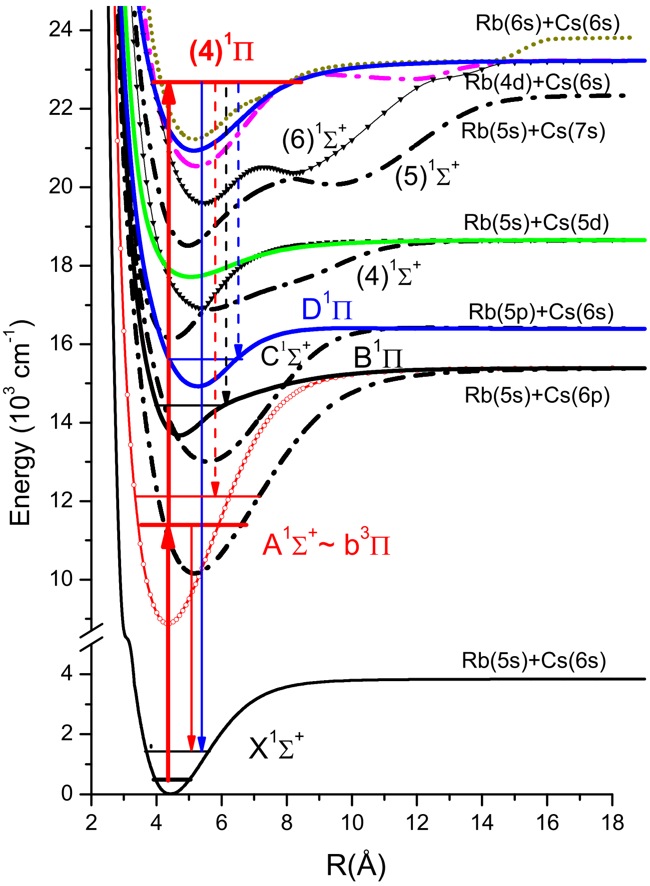

FIG. 1. Based on Ref. [6] schema of the singlet-state manifold of the RbCs molecule involved in the consideration. The solid vertical arrows show the two-step laser excitation of the (4) $^1\Pi$ state through an intermediate level of the singlet-triplet $A\,^1\Sigma^+ \sim b\,^3\Pi$ complex, as well as the observed LIF transitions. The dashed arrows denote the dominant (according to calculations) radiative decay channels of the (4) $^1\Pi$ state.

visible lines of an Ar$^+$ laser. There is a dense manifold of different symmetry states in the energy range of the (4) $^1\Pi$ state. Hence, the latter is expected to be subject to numerous perturbations, as it was observed for the (4) $^1\Pi$ state in KCs (see [17]). Therefore, we will refer to the (4) $^1\Pi$ state of RbCs as an entirely perturbed one.

In present study we extend spectroscopic information on the (4) $^1\Pi$ state significantly by recording high-resolution FT spectra of LIF excited by two-step laser excitation. In performing the experiments, a particular (4) $^1\Pi(v', J')$ rovibronic level is reached via an intermediate level of the fully mixed singlet-triplet $A\,^1\Sigma^+ \sim b\,^3\Pi$ complex, which was comprehensively studied in Ref. [18]. This makes it possible to predict with sufficient accuracy the required wave numbers of the first step of (4) $^1\Pi(v', J' = J; J \pm 1) \leftarrow A \sim b(E_{A\sim b}, J = J'' \pm 1) \leftarrow X\,^1\Sigma^+(v'', J'')$ excitation. The experimental term values are included in a direct potential fit (DPF) analysis applying the robust weighted nonlinear least-squares method [19] and the fully analytical expanded Morse oscillator (EMO) potential [20]. The obtained EMO PEC is additionally validated by comparing experimental LIF intensity distributions with the ones derived from the empirical potential. For this purpose, the *ab initio* electronic structure calculations are performed for the related states, along with estimates of radiative lifetimes and vibronic branching ratios. In addition, it appears possible to experimentally determine the Λ-splitting energies Δ_{ef} and relevant q factor as well as to compare the latter with a calculated value.

II. EXPERIMENT

Two-step excitation of the (4) $^1\Pi$ state of RbCs (see Fig. 1) was realized by two Ti: sapphire lasers MBR110 (Coherent). The singlet-triplet $A\,^1\Sigma^+ \sim b\,^3\Pi$ complex served as an intermediate state. Two copropagating laser beams were overlapped in the central part of the linear heat-pipe tube with rubidium and cesium metals operating at 300 °C. The heat pipe was filled with Ar buffer gas at about 2 mbars of pressure. The laser power varied from experiment to experiment, typically being within 300–500 mW for both lasers. The LIF spectra were recorded by a FT spectrometer (Bruker IFS 125HR) at instrumental resolution 0.03 cm^{-1}. A photomultiplier tube was used to detect the spectra in the range from 10 000 to 22 000 cm^{-1}. The laser frequency needed to excite in the first step a particular $A\,^1\Sigma^+ \sim b\,^3\Pi(E_{A\sim b}, J) \leftarrow X\,^1\Sigma^+(v'', J'')$ transition was determined from calculated term values $E_{A\sim b}$ of the $A\,^1\Sigma^+ \sim b\,^3\Pi$ complex, which, according to Refs. [16,18], can be predicted with an experimental accuracy of about 0.01 cm^{-1}. The ground $X\,^1\Sigma^+(v'', J'')$ level energies were calculated using the empirical PEC from Ref. [21].

The $A \sim b \to X$ LIF spectra in the range 6000–12 000 cm^{-1} were recorded and analyzed in order to find the optimal $A \sim b(E_{A\sim b}, J) \leftarrow X\,^1\Sigma^+(v'', J'')$ first step transition and to fine-tune the respective laser frequency. In this range the InGaAs diode was used for the infrared LIF detection.

At fixed first laser frequency ν_{L1}, the second laser was tuned over the range of (4) $^1\Pi \leftarrow A \sim b$ absorption bands, which were estimated using the Dunham molecular constants of the (4) $^1\Pi$ state from Ref. [10]. The appearance of two-step excitation was monitored by observation of the (4) $^1\Pi \to X$ LIF signal in the range around 20 000 cm^{-1} in the preview mode of the FT spectrometer. To catch a weaker two-step excitation, the observation of an illuminated area inside the heat pipe by eye through a blue filter was useful. Figure 2 shows the LIF spectrum, which demonstrates a two-step excitation of the (4) $^1\Pi(v' = 0)$ level with a characteristic single maximum in the (4) $^1\Pi(v' = 0) \to X\,^1\Sigma^+(v'')$ LIF intensity distribution (see the right side of the figure).

According to the plan of the experiment, we excited in the first step rotational levels of the $A \sim b$ complex with $J = 10$ and 40 of the ^{85}RbCs molecule. Hence, the observed rotational levels of the (4) $^1\Pi$ state in the second step excitation of P, R, and Q transitions possess $J' = 9$–11 and 39–41. However, LIF from a number of the (4) $^1\Pi$ levels with other J' values was also observed due to accidental resonances in the $A \sim b \leftarrow X$ and (4) $^1\Pi \leftarrow A \sim b$ transitions for the used frequencies of both lasers. In several cases two-step one-color excitation was observed. Moreover, as later analysis had shown, in some cases the laser nominated for the second step actually worked in the first step and vice versa.

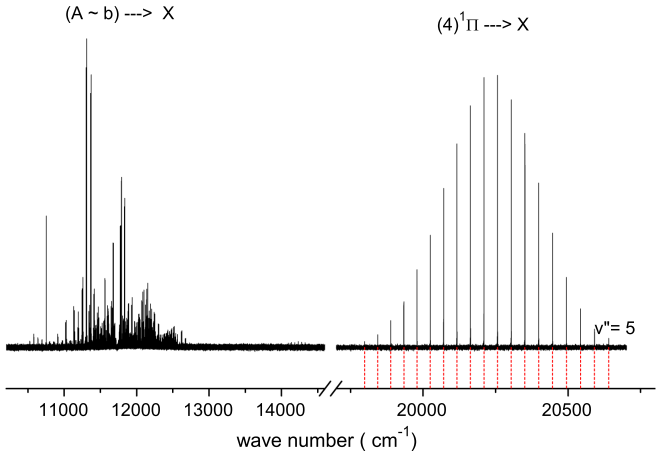

FIG. 2. Shown on the right is an example of a LIF spectrum (Q progression) representing two-step excitation of the $(4)\,^1\Pi$ state in transitions $(4)\,^1\Pi(v'=0, J'=10f, E'=20\,913.462\ \text{cm}^{-1}) \leftarrow A\,^1\Sigma^+ \sim b\,^3\Pi(E_{A\sim b}=10\,160.215\ \text{cm}^{-1}, J=10) \leftarrow X\,^1\Sigma^+(v''=4, J''=9)$. The laser frequencies are $\nu_{L1}=9935.917\ \text{cm}^{-1}$ and $\nu_{L2}=10\,753.243\ \text{cm}^{-1}$. On the left is a fragment of the respective $A\sim b\rightarrow X$ LIF spectrum.

Overall, about 50 LIF spectra containing the $(4)\,^1\Pi \rightarrow X\,^1\Sigma^+$ transition were recorded. Two progressions belonging to the ^{87}RbCs isotopologue were also assigned.

III. ANALYSIS OF SPECTRA

Assignment of LIF progressions $(4)\,^1\Pi \rightarrow X\,^1\Sigma^+$ was straightforward based on highly accurate vibrational and rotational differences of the ground X state [21]. Due to the presence of Ar buffer gas in the heat pipe, many satellite lines from collisionally populated neighboring rotational levels of both parity were observed around the strong lines, therefore many more term values of rovibronic levels of the $(4)\,^1\Pi$ state could be obtained. This is demonstrated in Fig. 3 by a P and R LIF progression recorded at two-step one-color excitation with a laser frequency of $10\,683.988\ \text{cm}^{-1}$. In the first step the laser excites the transition $A\,^1\Sigma^+ \sim b\,^3\Pi(E_{A\sim b}=10\,936.519\ \text{cm}^{-1}, J=116) \leftarrow X\,^1\Sigma^+(v''=0, J''=117)$ and in the second step it excites the $(4)\,^1\Pi(v'=19, J'=115e)$ level with energy $E'=21\,620.507\ \text{cm}^{-1}$. In Fig. 3(b) a zoomed-in fragment is shown with transitions to $v''_X=0$. Along with P and R satellite lines originating from e-parity levels, the Q lines from f-parity levels can be clearly distinguished. The energy difference between e and f components of a particular rovibrational level v', J' allows determination of Λ splitting Δ_{ef} and a respective experimental q factor:

$$\Delta_{ef} \equiv E^e_{v'J'} - E^f_{v'J'} = q^{\text{expt}}_{v'}[J'(J'+1)-1]. \tag{1}$$

However, the observed energy differences are very small and in most cases comparable with an accuracy of the line position determination being about 0.003–0.005 cm^{-1}. A crude estimate of the Δ_{ef} splitting for high rotational levels yielded a $q^{\text{expt}}_{v'}$ value of about $1.0\times10^{-6}\ \text{cm}^{-1}$.

It should be noted that the intensity of the Q_{115} line [see Fig. 3(b)] is about 20% less than that of Q lines from neighboring rotational levels Q_{114} and Q_{116}. This means that the collisional transfer of population from an optically excited rotational level J' with a particular parity to an opposite parity component of the same rotational level is less efficient than that of the collisional transfer to the neighboring $(J'\pm1)$ rotational levels. This effect took place in all cases when satellite lines from levels of both parities could be clearly distinguished.

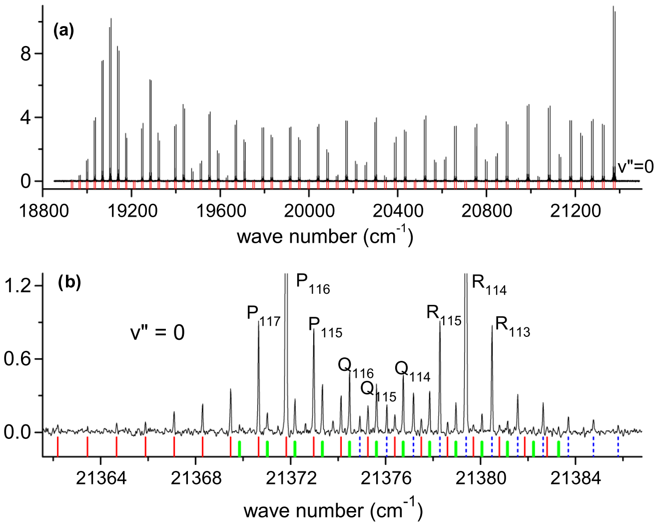

FIG. 3. Example of a LIF spectrum (P and R progression) representing two-step one-color excitation with laser frequency $\nu_{L1}\equiv\nu_{L2}=10\,683.988\ \text{cm}^{-1}$ in transitions $(4)\,^1\Pi(v'=19, J'=115e, E'=21\,620.507\ \text{cm}^{-1}) \leftarrow A\,^1\Sigma^+ \sim b\,^3\Pi(E_{A\sim b}=10\,936.519\ \text{cm}^{-1}, J=116) \leftarrow X\,^1\Sigma^+(v''=0, J''=117)$: (a) the entire spectrum and (b) close-up of a fragment with transitions to $v''=0$ with satellite lines due to collisional population of neighboring rotational levels of the upper state of both e and f parities. The red (solid), blue (dashed), and green (short) bars below the spectrum mark P, R, and Q lines, respectively. Indices denote the J'' value of the X state.

The resulting data field of the observed rovibronic $(4)\,^1\Pi$ state levels of both ^{85}RbCs and ^{87}RbCs isotopologues is presented in Fig. 4. It contains averaged over different measurements term values of 419 f and 332 e levels for ^{85}RbCs, as well as 18 f and 8 e levels for ^{87}RbCs. The data set spans vibrational levels v' from 0 to 44 and rotational levels J' from 9 to 251.

IV. ELECTRONIC STRUCTURE CALCULATIONS

The details of the present *ab initio* quasirelativistic calculation can be found elsewhere [22]. Briefly, the inner core shell of both rubidium and cesium atoms was replaced by the shape-consistent nonempirical effective core potentials [23], leaving nine outer shells (eight subvalence plus one valence) electrons for an explicit correlation treatment. The molecular orbitals were obtained from the solutions of the state-averaged complete active space self-consistent field problem for all 18 electrons on the lowest $(1\text{–}10)\,^{1,3}\Sigma^+$, $(1\text{–}6)\,^{1,3}\Pi$, and $(1\text{–}2)\,^{1,3}\Delta$ electronic states taken with equal weights [24]. The dynamical correlation energy was estimated by the internally contracted multireference configuration-interaction (MRCI)

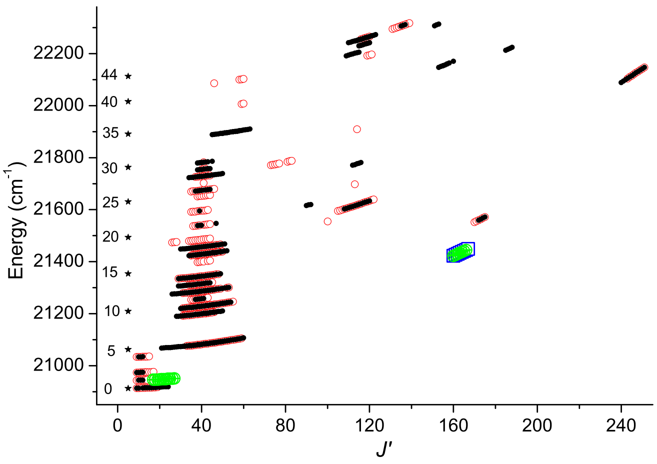

FIG. 4. Data field of experimentally observed (4) $^1\Pi$ state rovibrational levels as dependent on J'. Red open circles denote the e component of the ^{85}RbCs isotopologue, black closed circles denote the f component of the ^{85}RbCs, larger green closed circles denote the f component of the ^{87}RbCs isotopologue, blue open squares denote e component of the ^{87}RbCs isotopologue, and the column with stars denotes term values of the ^{85}RbCs isotopologue predicted with the present mass-invariant EMO potential for $J' = 5$.

method [25]. The MRCI procedure included all single and double excitations in the large $14a_1$, $8b_1$, $8b_1$, and $2a_2$ (in the C_{2v} symmetry) active space, however, it was applied for only two valence electrons keeping the 16 sub-valence electrons frozen.

The CPPs [26] of both atoms were exploited to account for the core-valence correlation effect implicitly. The Mueller-Meyer [27] damping functions are implemented in the present CPP construction. The required static dipole polarizabilities of the atomic cation α_c^+ were borrowed from Ref. [28], while the initial sets of the exponential cutoff parameter k_c (see Table I) were adjusted to reproduce experimental atomic energies [29] of the excited Rb($4\,^2D$) and Cs($7\,^2S$) states, respectively.

The adiabatic PECs of both singlet- and triplet-state manifolds of the RbCs molecule were calculated in the basis of spin-averaged electronic wave functions corresponding to the pure Hund's coupling case (a) [30], along with the singlet-singlet (4) $^1\Pi$–(1–7) $^1\Sigma^+$, (1–3) $^1\Pi$, (1–2) $^1\Delta$ electronic transition dipole moment (ETDM) functions $d_{ij}^{ab}(R)$. To clarify the origin of the Λ-doubling effect in the (4) $^1\Pi$ state, the L-uncoupling electronic matrix elements $L_{ij}^{ab}(R)$ between the (4) $^1\Pi$, (1–7) $^1\Sigma^+$, and (1–2) $^1\Delta$ states were evaluated as well.

According to the selection rule $\Delta\Omega = 0$ ($\Omega = \Lambda + \Sigma$) the singlet-triplet (4) $^1\Pi$–(1–4) $^3\Pi$, (1–7) $^3\Sigma^+$, (1–2)$^3\Delta$ spin-orbit-coupling (SOC) matrix elements $\xi_{ij}^{\text{so}}(R)$ between the individual quasirelativistic $|S, \Sigma, \Lambda\rangle$ eigenstates were evaluated by means of the corresponding spin-orbit part of the present effective core pseudopotentials. All calculations were performed in a wide range of the internuclear distances using the MOLPRO program suit [31].

TABLE I. Static electric dipole polarizabilities [28] α_c^+ and the exponential cutoff parameters k_c which are used to build the CPPs of Rb and Cs atoms. Both α_c^+ and k_c are given in a.u.

Atom	α_c^+	k_c
Rb	9.096	0.350
Cs	15.687	0.278

V. DIRECT POTENTIAL FIT PROCEDURE

A DPF analysis of the entirely perturbed (4) $^1\Pi$ state has been performed in the framework of the robust weighted nonlinear least-squares procedure [19] in order to diminish the undesirable impact of outliers caused by local perturbations. To constrain the modeling potential $U^{\text{emp}}(R)$ outside the experimental data region the corresponding χ^2 function included the difference-based PEC $U^*(R_i)$ [see Eq. (13) in Sec. VII A] of the (4) $^1\Pi$ state as well,

$$\chi^2 = \sum_{i=1}^{N_{\text{expt}}} \frac{\left(\delta_i^{\text{expt}}\right)^2}{\left(\sigma_i^{\text{expt}}\right)^2 + \left(\delta_i^{\text{expt}}\right)^2/3} + w\sum_{i=1}^{N_{ab}} \left(\frac{\delta_i^{ab}}{\sigma_i^{ab}}\right)^2,$$

$$\delta_i^{\text{expt}} = E_i^{\text{expt}} - E_i^{\text{calc}}, \quad \delta_i^{ab} = U^*(R_i) - U^{\text{emp}}(R_i), \tag{2}$$

where the empirical term values E_i^{calc} were calculated from the iterative numerical solution of the radial equation

$$\left(-\frac{\hbar^2 d^2}{2\mu d R^2} + U^{\text{eff}}(R) - E_i^{\text{calc}}\right)|v_i^J\rangle = 0, \tag{3}$$

with the effective interatomic potential $U^{\text{eff}}(R)$, which accounts for the Λ-doubling effect in the degenerate $^1\Pi$ state explicitly,

$$U^{\text{eff}} = U^{\text{emp}} + B[1 + sQB][J(J+1) - 1], \tag{4}$$

where $B(R) \equiv \frac{\hbar^2}{2\mu R^2}$ and $U^{\text{emp}}(R) = T_{\text{dis}} - D_e + U^{\text{EMO}}$ is the mass-invariant empirical potential taken in the fully analytical EMO form [20]

$$U^{\text{EMO}} = D_e\{1 - \exp[-\beta(R - R_e)]\}^2, \tag{5}$$

where D_e is the the well depth, R_e is the equilibrium distance, and the coefficient β,

$$\beta(R) = \sum_{i=0}^{N} \beta_i [y_p]^i, \quad y_p(R) = \frac{R^p - R_{\text{ref}}^p}{R^p + R_{\text{ref}}^p}, \tag{6}$$

is the polynomial function of the reduced radial coordinate y_p, with R_{ref} the reference distance and p the integer parameter.

The dimensionless scaling parameter s in Eq. (4) is equal to zero for the f-parity levels while it is considered as an adjusted parameter for the regularly perturbed levels of the e component. Here $Q(R)$ is the nonadiabatic correction function computed in advance by means of the *ab initio* adiabatic potentials $U_i^{ab}(R)$ and L-uncoupling electronic matrix elements $L_{ij}^{ab}(R)$ between the (4) $^1\Pi$ and (1–7) $^1\Sigma^+$ states obtained in Sec. IV:

$$Q(R) = 2\sum_{^1\Sigma^+} \frac{\left|L_{^1\Pi-^1\Sigma^+}^{ab}\right|^2}{U_{^1\Pi}^{ab} - U_{^1\Sigma^+}^{ab}}. \tag{7}$$

It should be noted that, according to the approximate sum rule [32], both the $Q(R)$ function and the scaling parameter s are

TABLE II. Comparison of equilibrium distance R_e and electronic energy T_e values available for the (4) $^1\Pi$ state of the RbCs molecule. The theoretical results correspond to the pure Hund's (a) coupling case. The abbreviation PW marks the present work.

Source	R_e (Å)	T_e (cm^{-1})
	Experiment	
PW	5.119	20896.905
[10]	5.117	20896.952
	Theory	
PW	5.15	20931
[34]	5.16	20959
[8]	5.13	20970
[33]	5.06	20977
[6]	5.08	21034
[9]	5.09	21294

related to the corresponding q factors as

$$q_v^{\rm calc} \approx s\langle v^J|BQB|v^J\rangle. \tag{8}$$

The uncertainties of experimental data $\sigma_i^{\rm expt}$ were taken equal to 0.005 cm^{-1} for all term values involved. The required uncertainties σ_i^{ab} in the *ab initio* difference-based potential $U^*(R)$ were estimated by a comparison with its previous theoretical counterparts [6,9,33] (see Table II). The weighting factor w in Eq. (2) was selected to be

$$w = \frac{\sum_{i=1}^{N_{\rm expt}} \left(\delta_i^{\rm expt}\right)^2/\left[\left(\sigma_i^{\rm expt}\right)^2 + \left(\delta_i^{\rm expt}\right)^2/3\right]}{\sum_{i=1}^{N_{ab}} \left(\delta_i^{ab}/\sigma_i^{ab}\right)^2} \tag{9}$$

in order to reach an equal balance between the contributions of experimental and theoretical data sets to the total χ^2 value.

VI. ESTIMATE OF RADIATIVE PROPERTIES

The reliability of the performed DPF analysis, which has been accomplished under the conventional adiabatic approximation using only the energy data set, was additionally tested by a comparison of the simulated relative intensity distributions in the long (4) $^1\Pi \rightarrow X\,^1\Sigma^+$ LIF progressions with their experimental counterparts. The corresponding rovibronic transition probabilities from rovibrational $v^{J'}$ levels of the (4) $^1\Pi$ state to rovibrational levels $v^{J''}$ of the ground $X\,^1\Sigma^+$ state were calculated as

$$I_{ij}^{\rm calc} \sim \nu_{ij}^4 \left|\langle v^{J'}|d_{ij}^{ab}|v^{J''}\rangle\right|^2,$$
$$\nu_{ij} = E_{v^{J'}} - E_{v^{J''}}, \tag{10}$$

where $i \in (4)\,^1\Pi$, $j \in X\,^1\Sigma^+$, and rovibrational eigenvalues $E_{v^{J'}}$ and eigenfunctions $|v^{J'}\rangle$ of the upper state were obtained by the solution of radial equation (3) with the present EMO potential, while the empirical potential $U_X^{\rm emp}$ was borrowed from Ref. [21] to calculate the corresponding $E_{v^{J''}}$ and $|v^{J''}\rangle$ of the ground X state. Here $d_{ij}^{ab}(R)$ is the *ab initio* ETDM function obtained for the (4) $^1\Pi \rightarrow X\,^1\Sigma^+$ transition in Sec. IV.

The spin-allowed ETDM functions $d_{ij}^{ab}(R)$ derived in Sec. IV between the (4) $^1\Pi$ state and lower-lying states manifold j denoting (1–4) $^1\Sigma^+$ and (1–2) $^1\Pi$ (see Fig. 1) were used to estimate radiative lifetimes τ_i and vibronic branching ratios R_{ij} of vibrational levels of the (4) $^1\Pi$ state:

$$\frac{1}{\tau_i^{\rm calc}} \approx \frac{8\pi^2}{3\hbar\epsilon_0}\langle v^{J'}|\sum_j \left[\Delta U_{ij}^{ab}\right]^3\left[d_{ij}^{ab}\right]^2|v^{J'}\rangle, \tag{11}$$

$$R_{ij}^{\rm calc} = \frac{8\pi^2}{3\hbar\epsilon_0}\langle v^{J'}|\left[\Delta U_{ij}^{ab}\right]^3\left[d_{ij}^{ab}\right]^2|v^{J'}\rangle\tau_i^{\rm calc}, \tag{12}$$

where $\Delta U_{ij}^{ab} = U_i^{ab}(R) - U_j^{ab}(R)$ is the difference of the *ab initio* PECs. Here the approximate sum rule [32] was used again to avoid summation over the bound part and integration over the continuum part of the vibrational spectra of the lower states.

VII. RESULTS AND DISCUSSION

A. *Ab initio* PECs, transition dipole moments, and *L*-uncoupling and spin-orbit-coupling matrix elements

All originally calculated adiabatic potentials $U_i^{ab}(R)$ for the (1–7) $^{1,3}\Sigma^+$, (1–4) $^{1,3}\Pi$, and (1–2) $^{1,3}\Delta$ states (except the ground X state) were transformed to the relevant difference-based PECs $U_i^*(R)$ by means of the semiempirical

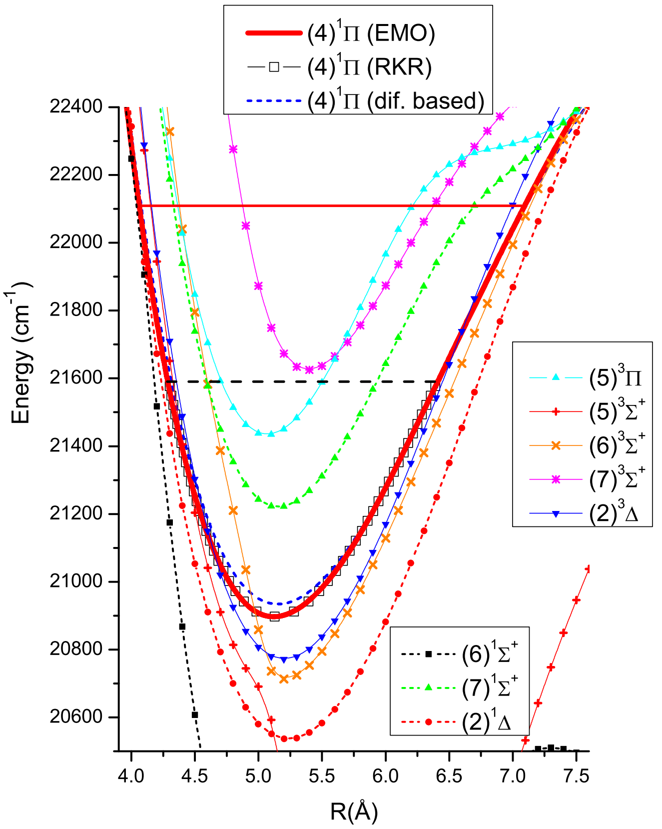

FIG. 5. Present calculated difference-based potentials of the (4) $^1\Pi$ state and of the states which are presumably responsible for both local and regular perturbations observed in the (4) $^1\Pi$ state. The present EMO PEC of the (4) $^1\Pi$ state is marked by a solid red (bold) line and the RKR potential from Ref. [10] is marked by open squares; the red solid horizontal line denotes the experiment-based region of the present EMO PEC, while the black dashed horizontal line refers to the RKR potential [10].

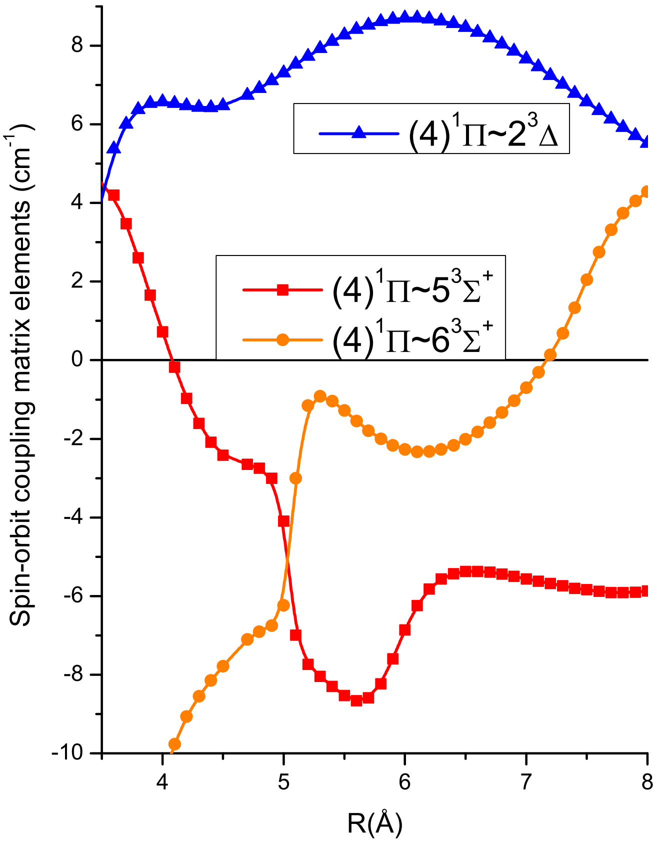

FIG. 6. The *ab initio* spin-orbit-coupling matrix element calculated between the singlet $(4)\,^1\Pi$ and triplet $(2)\,^3\Delta$ and $(5,6)\,^3\Sigma^+$ states of the RbCs molecule.

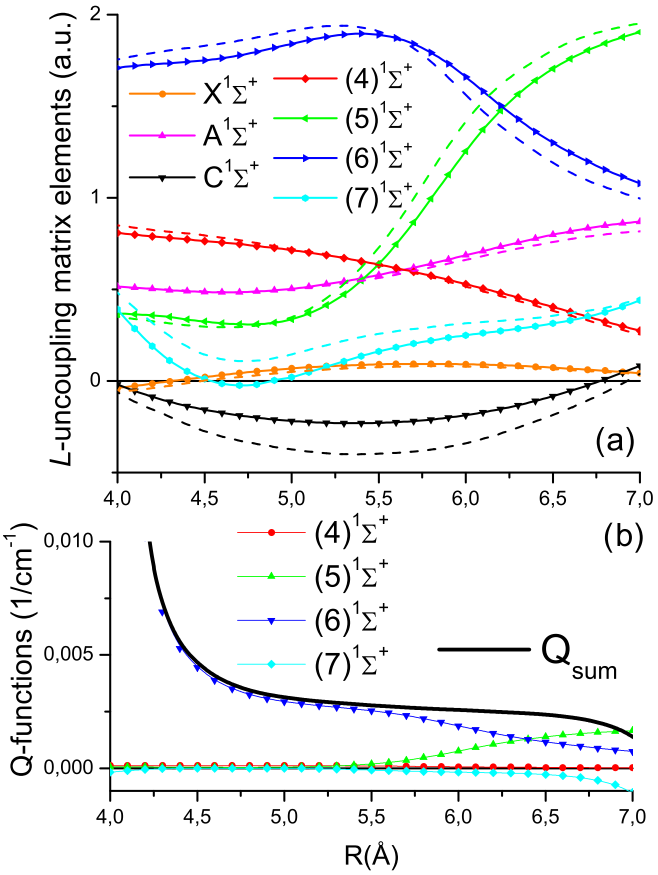

FIG. 7. (a) The *ab initio* *L*-uncoupling electronic matrix elements of the RbCs molecule evaluated between the $(4)\,^1\Pi$ state and the $(1–7)\,^1\Sigma^+$ states. The dashed lines denote the previous results obtained in the framework of the multipartition perturbation theory calculation in Ref. [34]. (b) The partial contribution of the $(4–7)\,^1\Sigma^+$ states in the sum-over-states $Q(R)$ function as defined by Eq. (7).

relation [34]

$$U_i^* = \left[U_i^{ab} - U_X^{ab}\right] + U_X^{\text{emp}} \qquad (13)$$

in order to diminish a basis set superposition error in the originally calculated *ab initio* PECs $U_i^{ab}(R)$ for the excited electronic states. Here $U_X^{\text{emp}}(R)$ is the highly accurate empirical PEC available for the ground $X\,^1\Sigma^+$ state [21] of RbCs in a wide R range. The singlet-state–triplet-state manifold located in the vicinity of the $(4)\,^1\Pi$ state is depicted in Fig. 5. Equilibrium constants R_e and T_e obtained from the present difference-based potential of the $(4)\,^1\Pi$ state are provided in Table II along with other sources. Note that the nearby lying triplet $(5,6)\,^3\Sigma^+$ and $(2)\,^3\Delta$ states intersect both repulsive and attractive walls of the $(4)\,^1\Pi$ state PEC.

The relevant spin-orbit-coupling electronic matrix elements are shown in Fig. 6. The sharp R dependence of the $(4)\,^1\Pi–(5)\,^3\Sigma^+$ and $(4)\,^1\Pi–(6)\,^3\Sigma^+$ SOC matrix elements observed near the point at $R_c \approx 5.1$ Å is attributed to the avoided crossing effect taking place between the adiabatic $(5)\,^3\Sigma^+$ and $(6)\,^3\Sigma^+$ states (see Fig. 5).

The L-uncoupling matrix elements between the $(4)\,^1\Pi$ and the first seven $(1–7)\,^1\Sigma^+$ states are depicted in Fig. 7(a). The present $L_{ij}^{ab}(R)$ functions are found to be very close to the previous results obtained in the framework of multipartition perturbation theory in Ref. [34]. The fractional contributions of the individual $^1\Sigma^+$ states to the total sum (7) are shown in Fig. 7(b). It can be seen that a dominant contribution to the Λ doubling of the $(4)\,^1\Pi$ state is caused by the interaction with the $(6)\,^1\Sigma^+$ state, which crosses the repulsive wall of the $(4)\,^1\Pi$ state near the point at $R_c \approx 4.1$ Å (see Fig. 5), while the contribution of the $(7)\,^1\Sigma^+$ state is almost negligible.

The calculated spin-allowed singlet-singlet $(4)\,^1\Pi–(1–6)\,^1\Sigma^+$, $(4)\,^1\Pi–(1–3)\,^1\Pi$, and $(4)\,^1\Pi–(1)\,^1\Delta$ ETDMs are presented in Fig. 8. Among them the $d_{ij}^{ab}(R)$ functions for $(4)\,^1\Pi–(2)A\,^1\Sigma^+$ and $(4)\,^1\Pi–(2)D\,^1\Pi$ transitions are predicted to be the strongest in intermediate internuclear distance range. The *ab initio* PECs, ETDM functions and L-uncoupling and SOC matrix elements are available in the Supplemental Material [35] in a pointwise form.

B. Experimental term values, *q* factors, and the empirical PEC

The overall nonaveraged $N_{\text{expt}} = 866$ experimental rovibronic term values E_i^{expt} assigned to both isotopologues and both e and f components were simultaneously involved in the present DPF analysis. The resulting mass-invariant parameters of the EMO potential obtained for the RbCs $(4)\,^1\Pi$ state are given in Table III. The EMO potential is presented in Fig. 5. As expected, the lower part of the present EMO PEC is very close to the RKR potential constructed in Ref. [10],

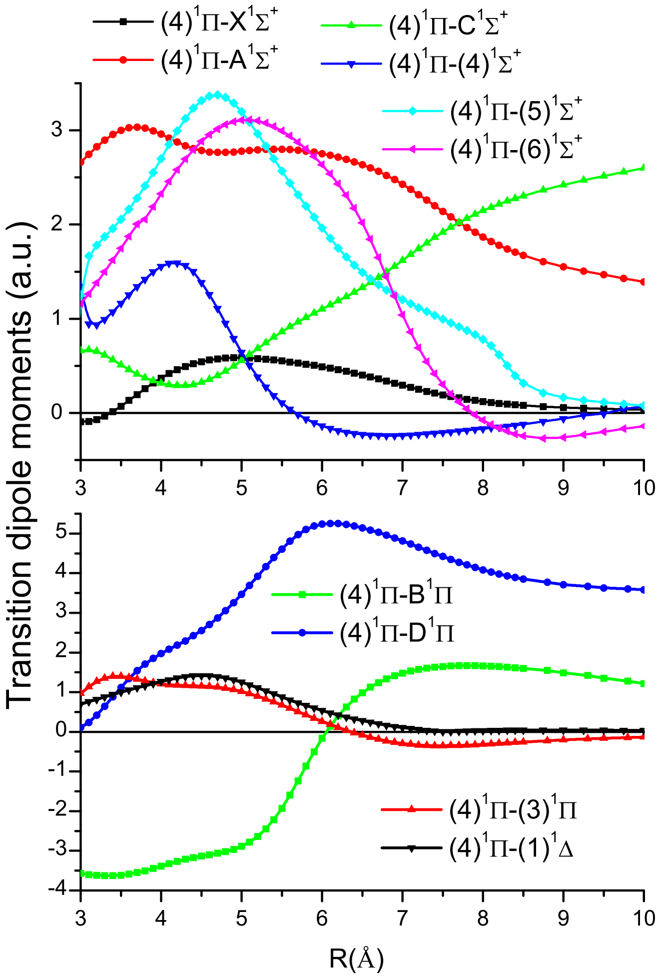

FIG. 8. The *ab initio* electronic transition dipole moments obtained between the $(4)\,^1\Pi$ state and the $(1–6)\,^1\Sigma^+$, $(1–3)\,^1\Pi$, and $(1)\,^1\Delta$ states of the RbCs molecule.

TABLE III. Resulting mass-invariant parameters of the empirical EMO potential (5) constructed for the RbCs $(4)^1\Pi$ state. Energies are given in cm^{-1}, the internuclear distance in Å, and the polynomial coefficients β_i in Å^{-1}. The parameters $T_{\mathrm{dis}} = 23\,191.503\ \mathrm{cm}^{-1}$, $p = 4$, and $R_{\mathrm{ref}} = 5.0$ Å were fixed during the fit. The numbers are truncated up to six decimal digits; the full values are given in the Supplemental Material [35].

Parameter	Value
D_e	2294.598
R_e	5.119042
β_0	0.555711
β_1	0.034720
β_2	−0.221238
β_3	1.129969
β_4	3.753468
β_5	−6.477096
β_6	−20.401909
β_7	18.648820
β_8	51.312053
β_9	−23.267061
β_{10}	−58.915683
β_{11}	9.920143
β_{12}	25.000342

the latter however being reliable in the more restricted energy region. The derived EMO PEC agrees well also with the present difference-based potential $U^*(R)$ and with most of the previous *ab initio* results (see Table II).

The differences between experimental and fitted rovibronic term values, or the residuals, are represented in Fig. 9(a) as dependent on vibrational quantum number v'. The experimental and fitted term values along with residuals are available in the Supplemental Material [35]. The significant residuals observed around $v' = 16, 25, 30, 38$, and 42 should apparently arise due to local nonadiabatic interactions with the $(2)\,^3\Delta$, $(5, 6)\,^3\Sigma^+$, and $(6)\,^1\Sigma^+$ states. In particular, the largest energy shifts exceeding 4 cm^{-1} for $v' = 25$ seem to be attributed to the pronounced SOC effect with the nearby triplet $(2)\,^3\Delta$ state (see Fig. 6). Unfortunately, a comprehensive deperturbation analysis of the $(4)\,^1\Pi$ state is strictly limited because of the fragmentary spectroscopic data available.

The empirical $q_{v'}^{\mathrm{emp}}$ factors obtained during the simultaneous DPF analysis of the experimental term values belonging to both e and f components are presented in Fig. 9(b). As expected, the fitted scaling parameter $s = 0.908$ involved in Eq. (4) is slightly less than 1 since the estimated sum-over-states Q function (7) obviously neglects the negative contributions of the higher-lying $(i > 7)\,^1\Sigma^+$ states. The $q_{v'}^{\mathrm{calc}}$ values estimated for $J' = 1$ levels by means of the approximate sum rule (8) and constrained $s \equiv 1$ parameter are slightly higher than their empirical counterparts. It should be noted that the present q values agree quite well with the previous theoretical q value $0.8 \times 10^{-6}\ \mathrm{cm}^{-1}$ reported in Ref. [34].

C. Intensity distributions, radiative lifetimes, and vibronic branching ratios

The measured and simulated relative intensity distributions of full $(4)\,^1\Pi(v', J') \rightarrow X\,^1\Sigma^+(v'')$ LIF progressions starting from the weakly and pronouncedly perturbed vibrational levels of the $(4)\,^1\Pi$ state of ^{85}RbCs isotopologue are presented in Figs. 10 and 11, respectively. In the case of doublet progressions, experimental intensity distributions of P and R branches were averaged while the corresponding theoretical intensities were obtained under the Q-branch $(J' = J'')$ approximation. Both measured and calculated intensities were normalized to the band with maximal experimental intensity.

Overall, very good agreement between the experimental intensities and their calculated counterparts takes place for weakly perturbed levels. The agreement is satisfactory even for the markedly nonadiabatically shifted levels. The LIF intensity distributions observed from low vibrational levels (for example, $v' = 2$ and 10 in Fig. 10) obey the Condon reflection principle [36] since the $I(v'')$ function is modulated by the square of the vibrational wave function $\chi(R) \equiv |v'\rangle$ of the upper state,

$$I(v'') \sim |\chi(R^*)|^2, \tag{14}$$

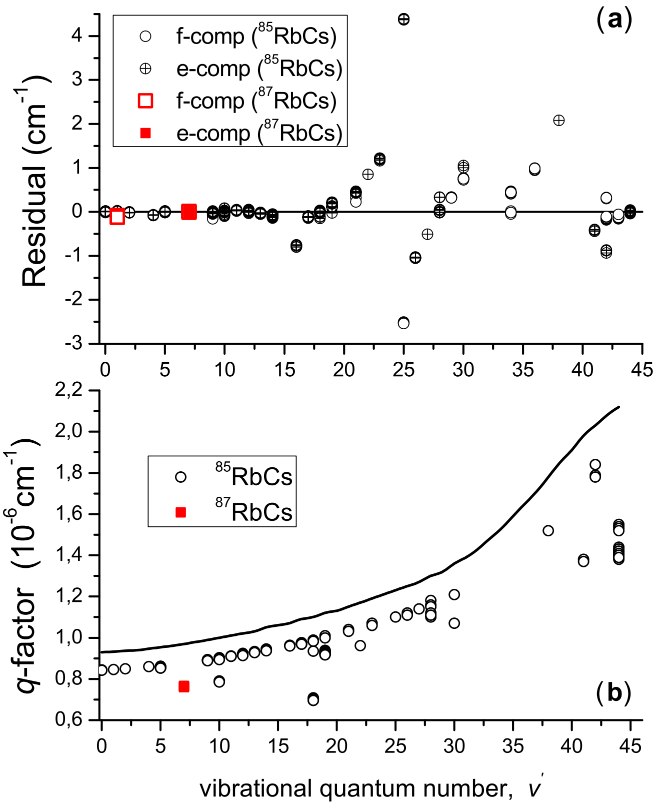

FIG. 9. (a) Differences between experimental and calculated by the present EMO PEC rovibronic term values of the RbCs (4) $^1\Pi$ state as dependent on the vibrational quantum number v'. (b) Open circles represent the empirical $q_{v'}$ factors obtained during the DPF analysis based on the EMO potential (5), the fixed *ab initio* $Q(R)$ function (7), and the fitted parameter $s = 0.908$; the solid line represents the theoretical $q_{v'}$ values predicted due to the approximate sum rule (8) for $J' = 1$ levels of the ^{85}RbCs isotopologue using the constrained $s \equiv 1$ parameter.

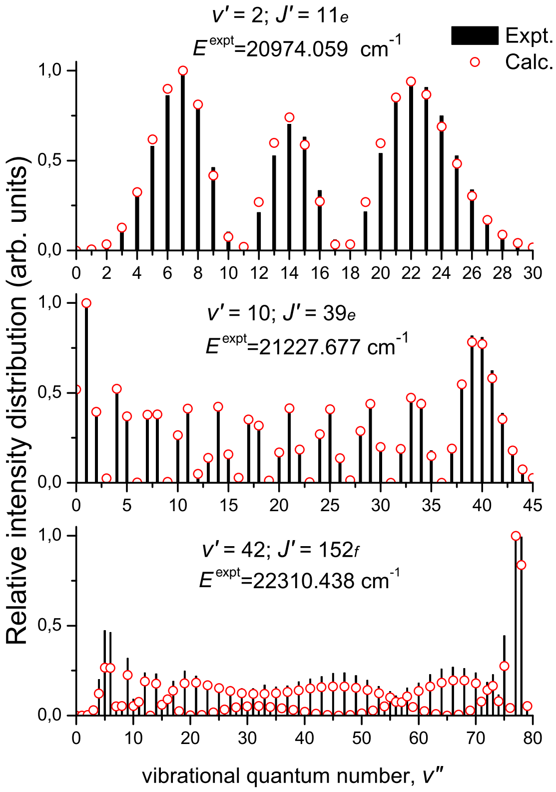

FIG. 10. Comparison of experimental and calculated relative intensity distributions in the full $(4)\,^1\Pi(v', J') \rightarrow X\,^1\Sigma^+(v'')$ LIF progressions starting from the weakly perturbed vibrational levels $v' = 2$, 10, and 42 of the (4) $^1\Pi$ state of the ^{85}RbCs isotopologue; the respective residuals between the experimental and calculated term values are -0.009, 0.01, and 0.332 cm^{-1}.

where the reflection point R^* is a single root of the transcendental equation

$$E_{v'} - U'(R^*) = E_{v''} - U''(R^*). \tag{15}$$

For high vibrational levels (e.g., $v' = 42$) the so-called interference structure of the LIF intensity takes place since Eq. (15) has multiple roots.

The calculated τ_i and R_{ij} values of the (4) $^1\Pi$ state are depicted in Fig. 12. As can be seen, the lifetime slowly increases as v' increases. The predicted τ values are by about 10 and 2 times smaller than the τ values calculated in Ref. [16] for the (3) $^1\Pi$ and (5) $^1\Sigma^+$ states, respectively. Furthermore, in contrast to the increasing τ values of the (4) $^1\Pi$ state, the radiative lifetimes of both (3) $^1\Pi$ and (5) $^1\Sigma^+$ states are rapidly decreasing with growing v'.

As expected, the dominant decay channel of the (4) $^1\Pi$ state is the infrared (IR) transition to the $A \sim b$ complex. However, in contrast to the case of (3) $^1\Pi$ and (5) $^1\Sigma^+$ states [16], the decay rate to the ground $X\,^1\Sigma^+$ state is only two times smaller than to the $A \sim b$ complex, therefore the visible $(4)\,^1\Pi \rightarrow X\,^1\Sigma^+$ LIF could be easily observed. The contribution of the far IR $(4)\,^1\Pi \rightarrow B, D\,^1\Pi$ transitions is almost the same as that of transitions to the ground state, the $(4)\,^1\Pi \rightarrow D\,^1\Pi$ channel being more efficient than the $(4)\,^1\Pi \rightarrow B\,^1\Pi$ channel.

VIII. CONCLUSION

We performed a high-resolution Fourier-transform spectroscopic study of the highly excited (4) $^1\Pi$ state of the RbCs molecule by applying two-step $(4)\,^1\Pi \leftarrow A\,^1\Sigma^+ \sim b\,^3\Pi \leftarrow X\,^1\Sigma^+$ optical excitation followed by observation of the collisionally enriched $(4)\,^1\Pi \rightarrow X\,^1\Sigma^+$ laser-induced fluorescence spectra. A summary of two-step excitation transitions exploited in the present experiment is provided in the Supplemental Material [35]. The direct potential fit of experimental rovibronic term values determined in the interval $v' \in [0, 44]$, $J' \in [9, 251]$ with an uncertainty of 0.005 cm^{-1} has revealed numerous shifts in the measured level positions with respect to their adiabatically (single-state) fitted counterparts. In contrast to the term value positions, the relative intensity distributions simulated for the measured $(4)\,^1\Pi \rightarrow X\,^1\Sigma^+$ LIF progressions agree well with their experimental counterparts even for the profoundly perturbed levels of the upper state. The sum-over-states Λ-doubling factors estimated for the (4) $^1\Pi$ state support their experimental counterparts as well.

We believe that the derived energies and radiative properties of the entirely perturbed (4) $^1\Pi$ state of the RbCs molecule

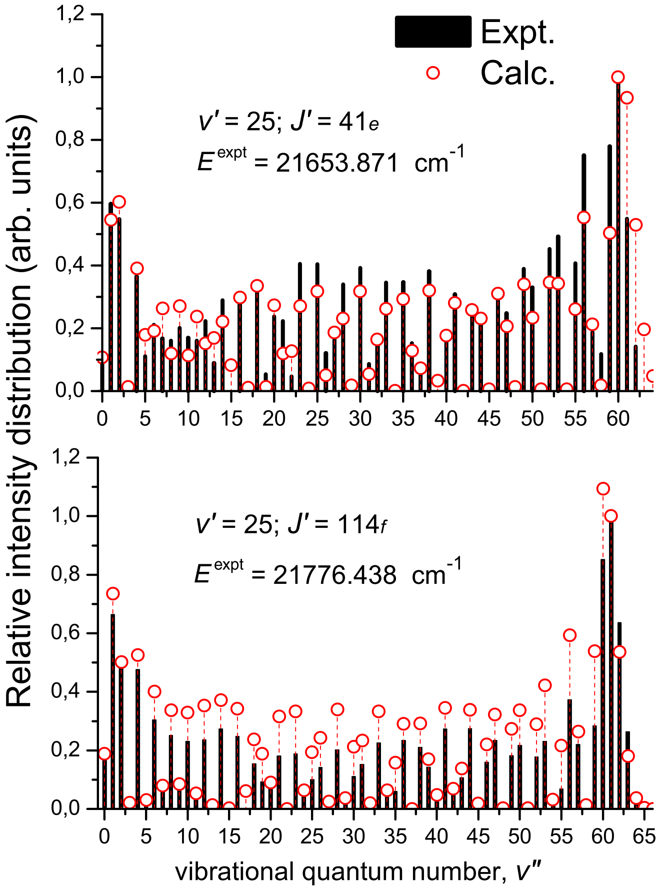

FIG. 11. Comparison of experimental and calculated relative intensity distributions in full $(4)\,^1\Pi(v'=25;J')\rightarrow X\,^1\Sigma^+(v'')$ LIF progressions starting from locally perturbed $J'=41$ and 114 rovibronic levels of the ^{85}RbCs isotopologue; the respective residuals between the experimental and calculated term values are 4.385 and -2.532 cm^{-1}.

will facilitate its future usage as an intermediate state in multistep laser-induced population transfer to both lower- (including the absolute ground state) and higher-lying states manifold. The present experimental and *ab initio* studies may serve as the first step to acquiring more abundant spectroscopic information, which will make it possible to perform a comprehensive deperturbation analysis of the $(4)\,^1\Pi$ state along with the neighboring interacting states.

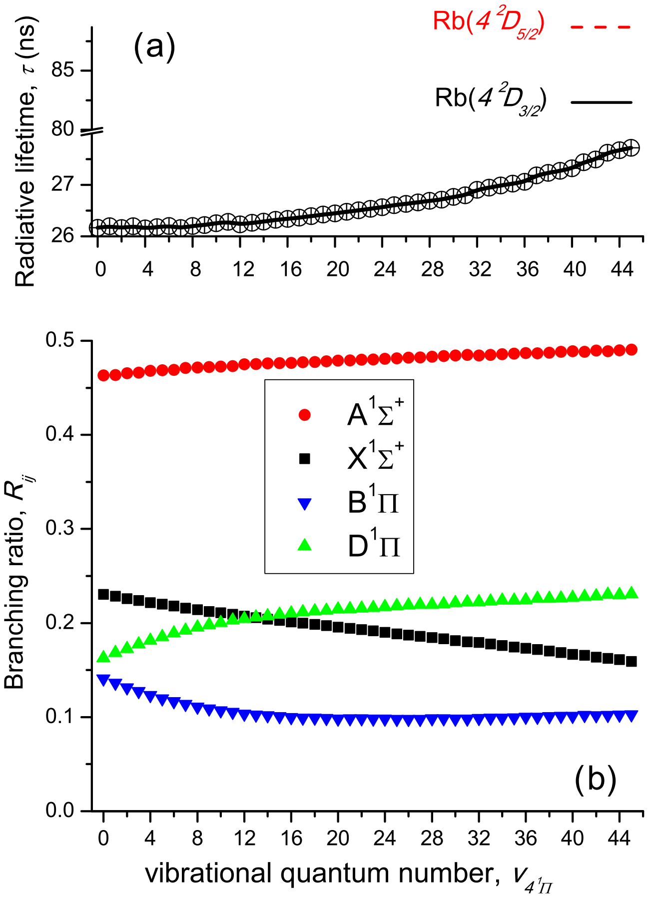

FIG. 12. (a) Radiative lifetimes and (b) vibronic branching ratios of vibrational levels v' of the ^{85}RbCs $(4)\,^1\Pi$ state evaluated using the present EMO PEC for the upper state as well as the corresponding *ab initio* ETDM functions and adiabatic PECs evaluated for the lower-lying singlet-state manifold by Eq. (12). The lifetimes of related atomic levels are presented in (a) by short solid lines.

ACKNOWLEDGMENTS

E.A.P. and A.V.S. are grateful for the support from Russian Foundation for Basic Research (RFBR) Grant No. 16-03-00529a. I.K., A.K., M.T., and R.F. acknowledge support from the Latvian Science Council Grant No. lzp-2018/1-0020: "Determination of structural and dynamic properties of alkali diatomic molecules for quantum technology applications" and from the University of Latvia Base Funding Grant No. Y5-AZ27. A.K. acknowledges support from Postdoctoral Grant No. 1.1.1.2/16/I/001, Proposal No. 1.1.1.2/I/16/068.

---

[1] T. Takekoshi, L. Reichsöllner, A. Schindewolf, J. M. Hutson, C. R. Le Sueur, O. Dulieu, F. Ferlaino, R. Grimm, and H.-C. Nägerl, Phys. Rev. Lett. **113**, 205301 (2014).

[2] P. K. Molony, P. D. Gregory, Z. Ji, B. Lu, M. P. Köppinger, C. R. Le Sueur, C. L. Blackley, J. M. Hutson, and S. L. Cornish, Phys. Rev. Lett. **113**, 255301 (2014).

[3] C. D. Bruzewicz, M. Gustavsson, T. Shimasaki, and D. DeMille, New J. Phys. **16**, 023018 (2014).

[4] T. Shimasaki, J.-T. Kim, and D. DeMille, Chem. Phys. Chem. **17**, 1 (2016).

[5] G. Quéméner and P. S. Julienne, Chem. Rev. **112**, 4949 (2012).

[6] A. R. Allouche, M. Korek, K. Fakherddin, A. Chaalan, M. Dagher, F. Taher, and M. Aubert-Frecon, J. Phys. B **33**, 2307 (2000).

[7] H. Fahs, A. R. Allouche, M. Korek, and M. Aubert-Frecon, J. Phys. B **35**, 1501 (2002).

[8] H. Souissi, S. Jellali, C. Maha, H. Habli, B. Oujia, and F. H. Gadéa, J. Quant. Spectrosc. Radiat. Transfer **200**, 173 (2017).

[9] I. S. Lim, W. C. Lee, Y. S. Lee, and G.-H. Jeung, J. Chem. Phys. **124**, 234307 (2006).

[10] T. Gustavsson, C. Amiot, and J. Vergès, Mol. Phys. **64**, 293 (1988).

[11] B. Kim and K. Yoshihara, Chem. Phys. Lett. **212**, 271 (1993).

[12] B. Kim and K. Yoshihara, J. Chem. Phys. **100**, 1849 (1994).

[13] Y. Yoon, Y. Lee, T. Kim, J. S. Ahn, Y. Jung, B. Kim, and S. Lee, J. Chem. Phys. **114**, 8926 (2001).

[14] Y. Lee, Y. Yoon, S. Lee, and B. Kim, J. Phys. Chem. A **113**, 12187 (2009).

[15] V. Zuters, O. Docenko, M. Tamanis, R. Ferber, V. V. Meshkov, E. A. Pazyuk, and A. V. Stolyarov, Phys. Rev. A **87**, 022504 (2013).

[16] K. Alps, A. Kruzins, O. Nikolayeva, M. Tamanis, R. Ferber, E. A. Pazyuk, and A. V. Stolyarov, Phys. Rev. A **96**, 022510 (2017).

[17] J. Szczepkowski, A. Grochola, W. Jastrzebski, and P. Kowalczyk, Chem. Phys. Lett. **576**, 10 (2013).

[18] A. Kruzins, K. Alps, O. Docenko, I. Klincare, M. Tamanis, R. Ferber, E. A. Pazyuk, and A. V. Stolyarov, J. Chem. Phys. **141**, 184309 (2014).

[19] J. K. G. Watson, J. Mol. Spectrosc. **219**, 326 (2003).

[20] R. J. Le Roy and A. Pashov, J. Quant. Spectrosc. Radiat. Transfer **186**, 210 (2016).

[21] O. Docenko, M. Tamanis, R. Ferber, H. Knöckel, and E. Tiemann, Phys. Rev. A **83**, 052519 (2011).

[22] E. A. Pazyuk, A. V. Zaitsevskii, A. V. Stolyarov, M. Tamanis, and R. Ferber, Russ. Chem. Rev. **84**, 1001 (2015).

[23] R. B. Ross, J. M. Powers, T. Atashroo, W. C. Ermler, L. A. LaJohn, and P. A. Christiansen, J. Chem. Phys. **93**, 6654 (1990).

[24] H.-J. Werner and P. J. Knowles, J. Chem. Phys. **82**, 5053 (1985).

[25] P. J. Knowles and H.-J. Werner, Theor. Chim. Acta **84**, 95 (1992).

[26] P. Fuentealba, H. Stoll, L. V. Szentpaly, P. Schwerdtfeger, and H. Preuss, J. Phys. B **16**, L323 (1983).

[27] W. Müller, J. Flesch, and W. Meyer, J. Chem. Phys. **80**, 3297 (1984).

[28] J. Mitroy, M. S. Safronova, and C. W. Clark, J. Phys. B **43**, 202001 (2010).

[29] NIST atomic data base, http://physics.nist.gov/.

[30] R. W. Field and H. Lefebvre-Brion, *The Spectra and Dynamics of Diatomic Molecules* (Elsevier, Amsterdam, 2004).

[31] H.-J. Werner, P. J. Knowles, G. Knizia, F. R. Manby, M. Schütz *et al.*, MOLPRO, version 2010.1, a package of *ab initio* programs, 2010, http://www.molpro.net.

[32] E. A. Pazyuk, A. V. Stolyarov, and V. I. Pupyshev, Chem. Phys. Lett. **228**, 219 (1994).

[33] D. Pavolini, T. Gustavsson, F. Spiegelmann, and J.-P. Daudey, J. Phys. B **22**, 1721 (1989).

[34] A. Zaitsevskii, E. A. Pazyuk, A. V. Stolyarov, O. Docenko, I. Klincare, O. Nikolayeva, M. Auzinsh, M. Tamanis, and R. Ferber, Phys. Rev. A **71**, 012510 (2005).

[35] See Supplemental Material at http://link.aps.org/supplemental/10.1103/PhysRevA.98.062517 for data files.

[36] M. S. Child, *Semiclassical Mechanics with Molecular Applications* (Clarendon, Oxford, 1991).

Correction: A grant number in the Acknowledgments contained an error and has been fixed.